

# Real-Space Spectral Approach to Orbital Magnetization

Kevin J. U. Vidarte,<sup>1,\*</sup> Henrique P. Veiga,<sup>2,3</sup> João M. Viana Parente Lopes,<sup>2</sup>  
Ramon Cardias,<sup>4</sup> Aires Ferreira,<sup>3</sup> Tarik P. Cysne,<sup>5</sup> and Tatiana G. Rappoport<sup>1,4,6,†</sup>

<sup>1</sup>*International Iberian Nanotechnology Laboratory (INL),  
Av. Mestre José Veiga, 4715-330 Braga, Portugal*

<sup>2</sup>*Centro de Física das Universidades do Minho e Porto Departamento de Física e Astronomia,  
Faculdade de Ciências, Universidade do Porto, 4169-007 Porto, Portugal*

<sup>3</sup>*School of Physics, Engineering and Technology and York Centre for Quantum Technologies,  
University of York, York YO10 5DD, United Kingdom*

<sup>4</sup>*Centro Brasileiro de Pesquisas Físicas (CBPF),  
Rua Dr Xavier Sigaud 150, Urca, 22290-180, Rio de Janeiro-RJ, Brazil*

<sup>5</sup>*Instituto de Física, Universidade Federal Fluminense, 24210-346 Niterói RJ, Brazil*

<sup>6</sup>*Physics Center of Minho and Porto Universities (CF-UM-UP), Campus of Gualtar, 4710-057, Braga, Portugal*  
(Dated: December 2, 2025)

We present a real-space spectral method for computing the orbital magnetization of crystals. Starting from the commutator form of the orbital magnetization operator, we formulate an energy-resolved spectral function that is amenable to exact Chebyshev polynomial expansions and yields the total magnetization upon integration up to the Fermi level. This avoids the need for computing eigenstates and ground-state projects, providing an efficient numerical framework that is applicable to very large systems even in the presence of disorder and temperature. Our approach is benchmarked on the Haldane model, finding results that are in excellent agreement with the modern  $k$ -space formulation of orbital magnetization. Leveraging this technique, we extend our study to systems with uncorrelated disorder and point defects, and further show that the bulk Chern number can be directly obtained from the magnetization spectral density. These results open a promising route to investigate orbital responses and topological transitions in real-space models of quantum materials with realistic complexity.

Orbital magnetization has become increasingly important in the study of topological quantum materials, where quantum metric and Berry curvature play a central role in shaping magnetic and transport properties. It has been identified as a key ingredient underlying the anomalous Hall effect in twisted graphene structures [1–3], certain topological magnets [4], and Weyl semimetals [5]. The orbital magnetization has also been suggested to play an important role in the emerging physics of altermagnets [6–8] and strongly correlated quantum materials [9–11], among other systems [12]. Thus, an accurate quantitative description of orbital magnetization is essential not only for interpreting magnetic measurements, but also electrodynamic responses to external fields [2, 4, 5], magneto-electric coupling [13, 14], and—more recently—the generation of orbital currents in the context of orbitronics [15–21].

Although great strides have been made in understanding orbital magnetization of crystals from a quantum perspective, its practical computation remains challenging. The modern theory expresses it as a bulk quantity, formulated as a Brillouin-zone integral over the set of occupied Bloch states and involving geometric quantities derived from Berry-phase theory [22–24]. This formulation has enabled closer agreement between theory and experiment in several elemental compounds [25, 26]. However, its im-

plementation in first-principles calculations is technically demanding: current approaches rely on Wannier interpolation, which requires constructing maximally localized Wannier functions and, when the relevant bands are not isolated, performing a disentanglement procedure that involves selecting suitable energy windows. These steps, while well established, add complexity and may introduce some uncertainty. In addition, the  $k$ -space formulation assumes translational invariance, limiting its applicability to systems with disorder, inhomogeneity, or large real-space supercells that arise naturally in realistic materials.

Real-space formulations offer an attractive alternative. A case in point is the theory of Bianco and Resta, which expresses the orbital magnetization in terms of a macroscopic average of a local magnetic dipolar density [27] and has been successfully applied to both insulating and metallic systems [28–30]. The real-space approach is naturally suited to disordered, inhomogeneous, and finite systems, and allows for a separation between bulk and surface contributions. However, this technique relies on constructing the ground-state one-body density matrix (and, hence, requires knowledge of the exact eigenstates), which severely limits its applicability to large systems and studies within real-space density-functional theory. Moreover, although a local *marker* for the orbital magnetization can be defined, only its average over a macroscopic region has a well-defined physical meaning [31].

In this work, we introduce a new real-space method for computing the orbital magnetization of any finite-size system based on the exact Chebyshev polynomial

\* kevin.urcia@inl.int

† tatiana.rappoport@inl.int

expansion of a spectral function [32–40] associated with the magnetization operator  $\mathcal{M}_z$ . Instead of finding the one-body density matrix of the occupied subspace by use of the ground-state projector, we construct a *spectral representation of the energy-resolved orbital magnetization density*, to be defined below, which gives access to the orbital magnetization of a sample through a simple numerical integration over energy. Our approach employs open boundary conditions, which avoids ambiguities associated with the position operator, while the use of Chebyshev expansions enables accurate investigations of realistic systems *without* diagonalization of the Hamiltonian matrix. For non-interacting models, the computation time scales linearly with system size [32, 35, 36], at fixed energy resolution [34], making it ideally suited for realistic computations of disordered materials and integration into first-principles workflows lacking explicit diagonalization [40]. In what follows, we validate the approach and discuss its advantages relative to existing reciprocal- and real-space formulations.

We start from the commutator form of the orbital magnetization for a finite two-dimensional system [27],

$$M_z = -\frac{ie}{2\hbar c A} \sum_{\epsilon_n < E_F} \langle \varphi_n | \mathbf{r} \times [\hat{H}, \mathbf{r}] | \varphi_n \rangle, \quad (1)$$

where  $A$  is the sample area,  $H$  is the single-particle Hamiltonian,  $\epsilon_n$  and  $|\varphi_n\rangle$  are the eigenvalues and eigenvectors of  $H$ , respectively, and  $E_F$  is the Fermi energy. The expectation value above may be written as  $M_z = \sum_{\epsilon_n < E_F} \langle \varphi_n | \hat{\mathcal{M}}_z | \varphi_n \rangle$ , where  $\hat{\mathcal{M}}_z = -ie(2\hbar c A)^{-1}(\hat{x}\hat{H}\hat{y} - \hat{y}\hat{H}\hat{x})$  is the orbital magnetization operator. We wish to show that this quantity can be computed without the need for explicit evaluation of the ground-state projector,  $\mathcal{P}_{\text{g.s.}} = \sum_{\epsilon_n < E_F} |\varphi_n\rangle\langle\varphi_n|$  [27]. One option is to directly expand Eq. (1) in Chebyshev polynomials. However, to avoid the step discontinuity of the Fermi-Dirac occupation function, we work instead with the spectral operator  $\hat{\mathcal{M}}_z \delta(E - H)$ , following the standard Chebyshev framework [32]. The crux of our approach is the *magnetization spectral density*,

$$m_z(E) = \text{Tr}[\hat{\mathcal{M}}_z \delta(E - \hat{H})]. \quad (2)$$

Knowledge of this quantity allows to retrieve the orbital magnetization via a straightforward and quick integration according to  $M_z(E_F) = \int^{E_F} m_z(E) dE$ . To efficiently evaluate  $m_z(E)$ , we expand  $\delta(E - H)$  in Chebyshev polynomials after rescaling  $\hat{H} \rightarrow \tilde{H}$  and  $E \rightarrow \tilde{E} \in [-1, 1]$ . The expansion coefficients are the moments  $\mu_n = \text{Tr}[\hat{\mathcal{M}}_z T_n(\tilde{H})]$ , computed iteratively via the Chebyshev recursion procedure. To further speed up the Chebyshev scheme, the traces are computed stochastically according to  $\mu_n \approx R^{-1} \sum_{r=1}^R \langle r | \hat{\mathcal{M}}_z T_n(\tilde{H}) | r \rangle$ , where  $|r\rangle$  is the  $r$ -th realization of a random vector [32]. The resulting expression for  $m_z(E)$  scales linearly with the number of random vectors  $R$ , number of lattice sites,  $D$ , and the number of Chebyshev iterations,  $M$ . This formulation

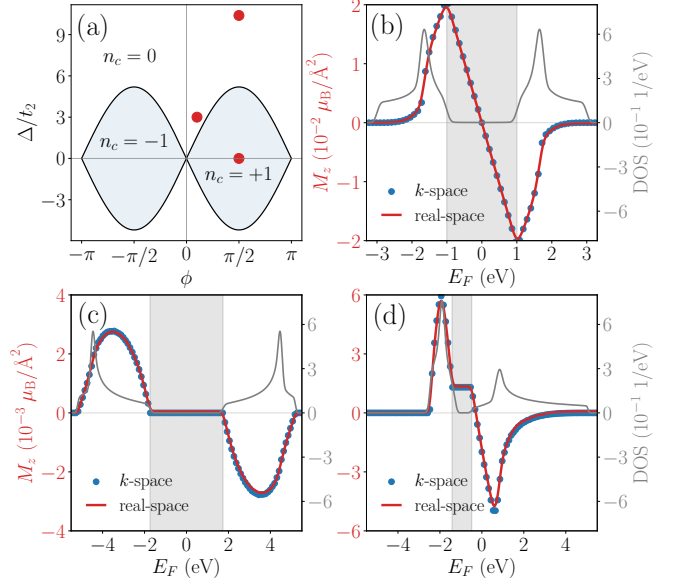


FIG. 1. (a) Topological phase diagram showing the Chern number of the bottom band as a function of  $\phi$  and  $\Delta/t_2$  ( $t_1 = 1$  eV and  $t_2 = t_1/3$ ). Red points  $(\phi, \Delta/t_2) = (0.5\pi, 0)$ ,  $(0.5\pi, 6\sqrt{3})$  and  $(0.1\pi, 3)$  indicate the parameters for panels (b), (c) and (d), respectively. (b-d) Orbital magnetization (red lines) in real-space formulation and density of states (gray lines) as functions of the energy. The blue dots show the results of the reciprocal-space formulation. In our Chebyshev approach, we simulate a large rectangular domain with  $10^6$  sites. Other parameters:  $M = 200$  and  $R = 800$ .

is fully equivalent to evaluating the zero-temperature expectation value equal to  $\text{Tr}[\hat{\mathcal{M}}_z \mathcal{P}_{\text{g.s.}}]$ , but bypasses the need for eigenstates or projection operators. It is therefore well suited for large-scale calculations of disordered systems and first-principles parametrized models. Furthermore, the spectral representation provides direct access to the magnetization spectral density, enabling analysis as a function of chemical potential and temperature [32].

To benchmark the method we use the Haldane model on the honeycomb lattice, a paradigmatic system for testing formulations of orbital magnetization [27, 41]. It is particularly convenient because tuning the sublattice imbalance  $\Delta$ , the complex next-nearest-neighbor (NNN) hopping  $t_2$ , and its phase  $\phi$  drives the system across topological phase transitions. For  $\phi = \pi/2$  the model is topologically nontrivial when  $|\Delta| < |3\sqrt{3}t_2|$  and trivial otherwise; at fixed  $\Delta = 0$  the topology can also be switched by varying  $\phi$ . In all regimes the system hosts a finite orbital magnetization, allowing a direct comparison between real- and  $k$ -space formulations and providing an ideal controlled setting where both trivial and topological contributions are captured.

The real-space lattice Hamiltonian reads

$$\hat{H} = -t_1 \sum_{\langle i,j \rangle} c_i^\dagger c_j + t_2 e^{i\phi} \sum_{\langle\langle i,j \rangle\rangle} \nu_{ij} c_i^\dagger c_j + \Delta \sum_i \xi_i c_i^\dagger c_i, \quad (3)$$

where  $t_1$  is the nearest-neighbor hopping,  $t_2 e^{i\phi}$  the complex NNN hopping with chirality  $\nu_{ij} = \pm 1$ , and  $\xi_i = \pm 1$  indicates the sublattice. For  $\phi = \pi/2$  the Dirac masses are  $m_K = \Delta - 3\sqrt{3}t_2$  and  $m_{K'} = \Delta + 3\sqrt{3}t_2$ , so the bulk gap closes at  $\Delta = \pm 3\sqrt{3}t_2$ , consistent with the phase diagram shown in Fig. 1(a).

Figures 1(b–d) compare  $M_z(E_F)$  (red) obtained from the spectral method on large rectangular flakes with open boundary conditions ( $708 \times 708$  unit cells, resulting in approximately  $10^6$  sites) with that from the modern theory expression in  $\mathbf{k}$ -space (blue). The density of states is also shown (gray) to help correlate orbital magnetization and electronic structure of the model. The agreement is excellent across topological and trivial insulating regimes. In the topological case where  $\phi = \pi/2$  and  $\Delta/t_2 = 0$  [Fig. 1(b)], the method reproduces the exactly linear dependence of  $M_z$  on  $E_F$  inside the bulk gap, a signature of the spectral flow of chiral edge states.

The in-gap linear behavior,  $M(E_F) \propto E_F$ , originates from a plateau-like feature in the magnetization spectral density (see SM [42]), which the Chebyshev expansion resolves accurately. The trivial phases [Figs. 1(c,d)] exhibit either a vanishing response inside the gap (electron–hole symmetric case) or a finite plateau when the anti-unitary particle-hole symmetry is broken, again in full quantitative agreement with  $\mathbf{k}$ -space calculations. A notable distinction relative to projector-based real-space formulations such as Ref. [27] is that our spectral approach captures the full contribution of the edge modes without suppressing or redistributing their weight. This allows us to reproduce not only the bulk part of the modern  $\mathbf{k}$ -space expression but also the topological boundary contribution, providing a complete match to the continuum formulation. While the local orbital magnetization operator,  $\hat{\mathcal{M}}_z(\mathbf{r})$ , *per se*, is gauge and origin dependent, its equilibrium expectation value over the entire sample is well defined and gauge invariant. Real-space maps (see SM [42]) show that a change in the origin redistributes weight between opposite edges in insulators and modifies the apparent edge–bulk partition in metallic regimes, without affecting the integrated  $M_z$ . This intrinsic difference between local and global quantities highlights both the utility and the limitations of real-space markers, and the advantage of focusing on the gauge-invariant spectral density. These features also highlight that in metallic systems the spatial maps of orbital magnetization cannot be interpreted without accounting for gauge and boundary conventions, and suggest that sample geometry may play a nontrivial role in itinerant orbital magnetism. Our real-space spectral method provides a unified and transparent framework for studying orbital magnetism by treating bulk and boundary responses on equal footing.

For the non-topological phases we consider two representative cases: one with electron–hole symmetry and one without, corresponding to Figs. 1(c) and (d). In the symmetric insulator ( $\phi = \pi/2$ ,  $\Delta/t_2 = 6\sqrt{3}$ ), the orbital magnetization vanishes inside the gap, whereas breaking electron–hole symmetry ( $\phi = 0.1\pi$ ,  $\Delta/t_2 = 3$ ) produces

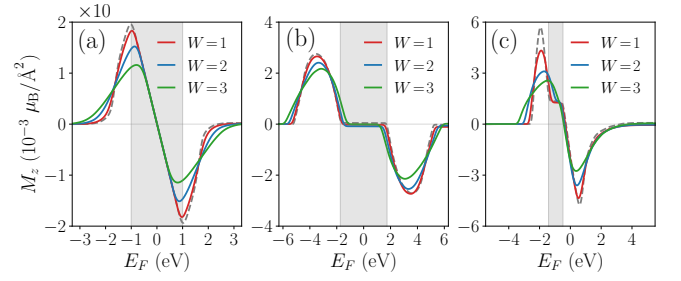


FIG. 2. Disorder effects in Haldane model: (a–c) Orbital magnetization with Anderson disorder as functions of the Fermi energy  $E_F$  for  $W = 1$  eV (red),  $W = 2$  eV (blue) and  $W = 3$  eV (green). The dashed gray lines correspond to the pristine systems. The panels (a), (b), and (c) refer to the red points in  $(\phi, \Delta/t_2) = (0.5\pi, 0)$ ,  $(0.5\pi, 6\sqrt{3})$ , and  $(0.1\pi, 3)$  of Fig. 1(a).

a finite plateau in  $M_z(E_F)$ . In both regimes the magnetization spectral density  $m_z(E)$  is zero inside the gap and only states localized near the physical boundaries contribute to the global magnetization (see SM [42]). In the metallic regime the average magnetization receives long-range contributions and a gauge-dependent mixture of edge-like and bulk-like character, consistent with the expected spectral behavior away from a gap.

The utility of our spectral method becomes especially clear when disorder is introduced. Because only sparse matrix–vector multiplications are required to construct the Chebyshev polynomials,  $T_n(\tilde{H})$ , the total computational cost scales linearly with the system size and number of Chebyshev iterations. This allows unprecedented calculations with up to  $10^{10}$  sites—including strongly disordered or inhomogeneous geometries—without diagonalization or projectors [35]. Anderson disorder therefore provides an ideal setting to demonstrate the strengths of our new approach in large systems of realistic complexity.

We introduce Anderson disorder as  $\hat{H} \rightarrow \hat{H} + \sum_i \varepsilon_i c_i^\dagger c_i$  with  $\{\varepsilon_i\}$  denoting random on-site energies drawn from a uniform distribution on the interval  $[-W/2, W/2]$ . Figures 2(b–d) show the evolution of  $M_z(E_F)$  for increasing  $W$ . In the topological insulating phase the linear dependence of  $M_z(E_F)$  within the gap remains essentially unchanged as long as the mobility gap persists, demonstrating the robustness of the boundary spectral flow. For the large-gap trivial insulator the magnetization remains zero in the gap for all  $W$ , whereas for smaller gaps the plateau shrinks and eventually disappears when disorder-induced states fill the gap. Local magnetization maps further confirm that the space-resolved orbital magnetization,  $\langle \hat{\mathcal{M}}_z(\mathbf{r}) \rangle$ , remains extended in the topological case, while trivial phases display isolated, disorder-induced islands that persist only when the gap is large (see SM [42]). These results confirm that the orbital magnetization of insulators is a bulk quantity, even when its real-space distribution is sensitive to gauge choice.

A central conceptual result is the link between the en-

ergy derivative of the orbital magnetization and the bulk Chern number,  $\mathcal{C}$  [27]. Within our formulation, this link can be expressed in a more direct way through the orbital magnetization spectral density defined in Eq. (2):

$$-\frac{2\hbar c}{e} m_z(E_F) = \frac{\mathcal{C}}{2\pi},$$

where  $\mathcal{C}$  denotes the Chern number of occupied states. Figure 3(a) shows  $-m_z(E_F) = -dM_z/dE_F$  for several parameter values near the  $\mathcal{C} = 0 \rightarrow 1$  transition of the Haldane model. We use this property to test the method in the vicinity of the topological transition of the Haldane model. We select several points near the  $\mathcal{C} = 0 \rightarrow 1$  phase boundary at fixed  $\Delta/t_2 = 3\sqrt{3}\sin(\pi/4)$  and varying  $\phi$ , and evaluate  $m_z$  at the charge-neutrality point (CNP), to ensure that  $E_F$  lies within the gap [Fig. 3(a)]. In the thermodynamic limit the transition occurs at  $\phi = 0.25\pi$ ; in finite systems the change is necessarily smooth, and our results follow this expected behavior. The plateaus reproduce the expected integer Chern numbers, and the transition sharpens with increasing system size [Fig. 3(b)], as expected in finite-size topological systems. For  $\phi < 0.25\pi$  we obtain  $\mathcal{C} \simeq 0$ , while for  $\phi > 0.25\pi$  we recover  $\mathcal{C} \simeq 1$ . As the system size increases, the crossover sharpens accordingly. Importantly, the Chern number is extracted here without projectors, curvature markers, Wannier functions, or assumptions about translational symmetry, in contrast with existing real-space approaches [43–45].

In the presence of disorder [Fig. 3(c)], the plateaus broaden, however, the method can still distinguish the two different topological phases for systems with well defined gaps. Disorder also helps to converge the Chebyshev expansion to the  $\mathcal{C}$  of the thermodynamic limit at the critical point of the topological phase transition for finite systems. Panel Fig. 3(d) shows the convergence of the Chern number as a function of the number of Chebyshev moments  $M$  in the expansion.

We turn now to vacancy defects, which generate qualitatively different physics from Anderson disorder [37]. Vacancies produce mid-gap resonances whose structure depends sensitively on particle-hole symmetry [34] and on whether the system is topological or trivial. In topological insulators on the honeycomb lattice, single vacancies are known to bind zero or near-zero modes with wave functions strongly peaked around the defect and hybridized with the chiral edge manifold [46]. These resonances do not produce in-gap extended states, but instead appear as sharp peaks near the band edges or at  $E = 0$  in systems with approximate chiral symmetry, consistent with our density of states in Fig. 4(a). Their spectral weight originates from the same subspace responsible for the boundary contribution to the orbital magnetization, and therefore affects the linear dependence of  $M_z(E_F)$  in a very characteristic way.

To explore this regime, we consider a vacancy concentration of 4% in a rectangular flake with  $10^6$  lattice sites. In the pristine topological phase ( $\phi = \pi/2$ ,  $\Delta/t_2 = 0$ ),

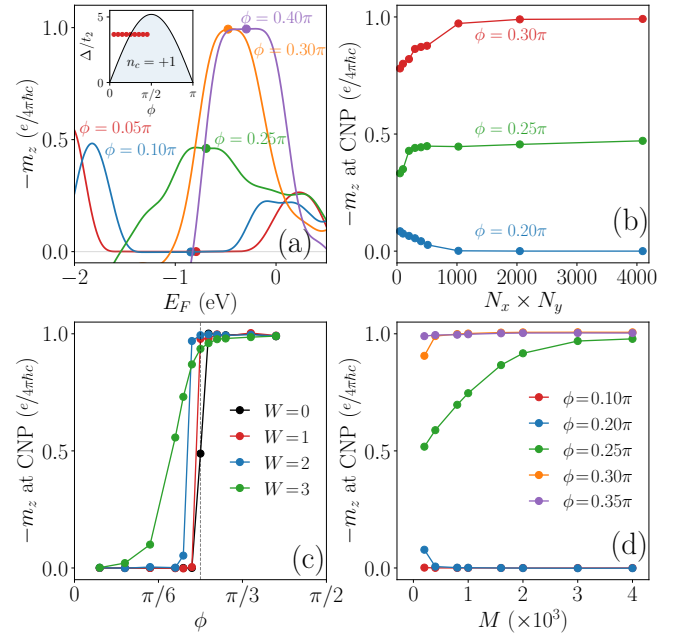


FIG. 3. Chern number from the orbital magnetization: Panel (a) plots  $-m_z$ , calculated within the band gap for pristine systems at  $\Delta/t_2 = 3\sqrt{3}\sin(\pi/4)$  and  $\phi = 0.05\pi, 0.10\pi, 0.25\pi, 0.30\pi$  and  $0.40\pi$ . The colored dots on each curve denote the respective CNP values. Other simulation parameters:  $D \approx 4 \times 10^6$ ,  $M = 200$  and  $R = 2000$ . The inset represents the Chern number of the valence band of the Haldane model. The red points in this phase diagram are relevant for the subsequent discussion and figures. Panel (b) plots  $-m_z$  at the CNP as a function of the sample sizes for pristine systems with  $\phi = 0.20\pi, 0.25\pi$  and  $0.30\pi$ . The panel (c) plots  $-m_z$  at the CNP as functions of  $\phi$  with  $D \approx 4 \times 10^6$ ,  $M = 4000$  and  $R = 2000$ . The panel (d) plots  $-m_z$  at the CNP as functions of  $M$  for  $W = 1$  with  $D \approx 4 \times 10^6$  and  $R = 2000$ .

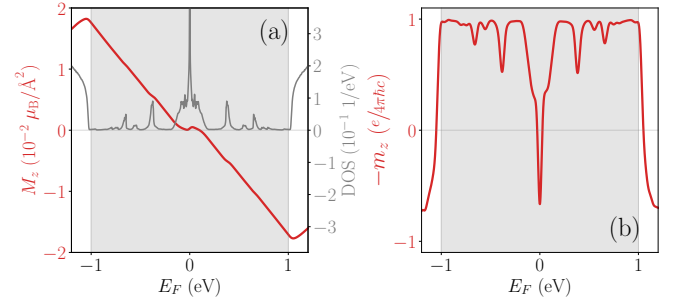


FIG. 4. Point defects in the Haldane model: Panel (a) plots the orbital magnetization (red line) in real-space formulation and density of states (gray line) as functions of the energy, within the band gap for the topological insulating phase with 4% vacancy concentration,  $\phi = 0.5\pi$  and  $\Delta/t_2 = 0$ . Panel (b) plots  $-m_z$ , calculated within the band gap for the same topological insulating phase. Other simulation parameters:  $D \approx 10^6$ ,  $M = 800$  and  $R = 2400$ .

the orbital magnetization displays a perfectly linear dependence inside the bulk gap. With vacancies, this lin-



earity survives almost entirely: it is disrupted only in narrow energy windows centered at the vacancy-induced resonances. Each in-gap (or near-edge) peak in the density of states produces a corresponding kink or inflection in  $M_z(E_F)$ , reflecting the sensitivity of the boundary magnetization to the sharp redistribution of spectral weight. The resonance near  $E = 0$  generates the strongest deviation, forming an odd-symmetric feature reminiscent of the zero-mode physics of graphene vacancies.

Surprisingly, the global trend of  $M_z$ —including the overall slope associated with the Chern number—remains intact even in the presence of relatively dense vacancy disorder, while the global topology encoded in the average Chern number is strongly affected near the resonances [see Fig. 4(b)]. This indicates that (i) the orbital magnetization is robust to vacancy scattering, and (ii) the vacancy resonances, although strongly localized, couple only weakly to the long-range orbital circulation that determines the macroscopic magnetization. As a consequence, the Chebyshev-based real-space approach can resolve both types of contributions simultaneously: the sharp, defect-induced resonances and the robust topological linear background.

In summary, we introduced a fully real-space formulation of orbital magnetization based on the Chebyshev expansion of the spectral operator  $\hat{\mathcal{M}}_z \delta(E - \hat{H})$ . This method avoids projectors and eigenstates entirely, works naturally with open boundaries, and scales linearly with system size, enabling simulations investigations of orbital magnetization in systems far more realistic and larger than those accessible to existing approaches. Because

the formulation remains valid in the presence of disorder and spatial inhomogeneities, it captures the evolution of orbital magnetization under uncorrelated on-site disorder and vacancy-induced resonances, revealing the conditions under which the topological signatures of the orbital magnetization can be considered to be robust. These results establish the Chebyshev spectral approach as a compact, computationally cheap, and broadly applicable framework for orbital magnetization in large, disordered, and topological systems.

## ACKNOWLEDGMENTS

TGR, JMVPL and AF acknowledge the FCT - Fundação para a Ciência e Tecnologia for financial support (Grant No. 2023.11755.PEX and DOI identifier <https://doi.org/10.54499/2023.11755.PEX>) TGR acknowledges FCT project reference numbers UIDB/04650/2020, and 2022.07471.CEECIND/CP1718/CT0001 (with DOI identifier: [10.54499/2022.07471.CEECIND/CP1718/CT0001](https://doi.org/10.54499/2022.07471.CEECIND/CP1718/CT0001)) and CNPq (Grant No 305013/2024-6). TGR and KJUV acknowledge support from the EIC Pathfinder OPEN grant 101129641 “OBELIX”. TPC acknowledges CNPq (Grant No. 305647/2024-5). HPV, JMVPL and AF acknowledge the University of York High-Performance Computing service, Viking. Further support from FCT through the PhD Grant. No. 2024.00560.BD (HPV) is acknowledged.

- 
- [1] A. L. Sharpe, E. J. Fox, A. W. Barnard, J. Finney, K. Watanabe, T. Taniguchi, M. A. Kastner, and D. Goldhaber-Gordon, Emergent ferromagnetism near three-quarters filling in twisted bilayer graphene, *Science* **365**, 605 (2019).
  - [2] J. Liu, Z. Ma, J. Gao, and X. Dai, Quantum valley hall effect, orbital magnetism, and anomalous hall effect in twisted multilayer graphene systems, *Phys. Rev. X* **9**, 031021 (2019).
  - [3] C. L. Tschirhart, M. Serlin, H. Polshyn, A. Shragai, Z. Xia, J. Zhu, Y. Zhang, K. Watanabe, T. Taniguchi, M. E. Huber, and A. F. Young, Imaging orbital ferromagnetism in a moiré chern insulator, *Science* **372**, 1323 (2021).
  - [4] R. Mei, Y.-F. Zhao, C. Wang, Y. Ren, D. Xiao, C.-Z. Chang, and C.-X. Liu, Electrically controlled anomalous hall effect and orbital magnetization in topological magnet  $\text{MnBi}_2\text{Te}_4$ , *Phys. Rev. Lett.* **132**, 066604 (2024).
  - [5] A. Nakamura, S. Nishihaya, H. Ishizuka, M. Kriener, Y. Watanabe, and M. Uchida, In-plane anomalous hall effect associated with orbital magnetization: Measurements of low-carrier density films of a magnetic weyl semimetal, *Phys. Rev. Lett.* **133**, 236602 (2024).
  - [6] C. C. Ye, K. Tenzin, J. Sławińska, and C. Autieri, Dominant orbital magnetization in the prototypical altermagnet mntc, *arXiv:2505.08675 [cond-mat.mtrl-sci]* (2025).
  - [7] S. Sorn and Y. Mokrousov, Activation of anomalous hall effect and orbital magnetization by domain walls in altermagnets, *arXiv:2505.15894 [cond-mat.mes-hall]* (2025).
  - [8] H. Bangar, P. Tsipas, P. Rout, L. Pandey, A. Kalaboukhov, A. Lintzeris, A. Dimoulas, and S. P. Dash, Interplay between altermagnetic order and crystal symmetry probed using magnetotransport in epitaxial altermagnet mntc, *arXiv:2505.14589 [cond-mat.mtrl-sci]* (2025).
  - [9] X. Liu, C. Wang, X.-W. Zhang, T. Cao, and D. Xiao, Orbital magnetization in correlated states of twisted bilayer transition metal dichalcogenides, *arXiv:2510.01727 [cond-mat.mes-hall]* (2025).
  - [10] J. Zhu and C. Huang, Magnetic-field-induced geometric response of mean-field projectors: Streda formula and orbital magnetization, *arXiv:2510.07001 [cond-mat.mes-hall]* (2025).
  - [11] J. Kang, M. Wang, and O. Vafeek, Orbital magnetization and magnetic susceptibility of interacting electrons, *arXiv:2509.20626 [cond-mat.str-el]* (2025).
  - [12] L. L. Lage, T. P. Cysne, and A. Latgé, Orbital magnetization in sierpinski fractals, *arXiv:2510.14556 [cond-mat.mtrl-sci]* (2025).
  - [13] X. Lu, R. Jiang, Z. Guo, and J. Liu, Orbital magnetoelectric coupling of three dimensional chern insulators, *npj Quantum Materials* **10**, 76 (2025).
  - [14] A. Malashevich, I. Souza, S. Coh, and D. Vanderbilt,

- Theory of orbital magnetoelectric response, *New Journal of Physics* **12**, 053032 (2010).
- [15] S. Bhowal and S. Satpathy, Intrinsic orbital and spin hall effects in monolayer transition metal dichalcogenides, *Phys. Rev. B* **102**, 035409 (2020).
  - [16] T. P. Cysne, S. Bhowal, G. Vignale, and T. G. Rappoport, Orbital hall effect in bilayer transition metal dichalcogenides: From the intra-atomic approximation to the bloch states orbital magnetic moment approach, *Phys. Rev. B* **105**, 195421 (2022).
  - [17] A. Pezo, D. García Ovalle, and A. Manchon, Orbital hall physics in two-dimensional dirac materials, *Phys. Rev. B* **108**, 075427 (2023).
  - [18] O. Busch, I. Mertig, and B. Göbel, Orbital hall effect and orbital edge states caused by  $s$  electrons, *Phys. Rev. Res.* **5**, 043052 (2023).
  - [19] H. Liu, J. H. Cullen, D. P. Arovas, and D. Culcer, Quantum correction to the orbital hall effect, *Phys. Rev. Lett.* **134**, 036304 (2025).
  - [20] T. P. Cysne, L. M. Canonico, M. Costa, R. B. Muniz, and T. G. Rappoport, Orbitronics in two-dimensional materials, *npj Spintronics* **3**, 39 (2025).
  - [21] A. Veneri, T. G. Rappoport, and A. Ferreira, Extrinsic orbital hall effect: Orbital skew scattering and crossover between diffusive and intrinsic orbital transport, *Phys. Rev. Lett.* **134**, 136201 (2025).
  - [22] D. Xiao, J. Shi, and Q. Niu, Berry phase correction to electron density of states in solids, *Phys. Rev. Lett.* **95**, 137204 (2005).
  - [23] T. Thonhauser, D. Ceresoli, D. Vanderbilt, and R. Resta, Orbital magnetization in periodic insulators, *Phys. Rev. Lett.* **95**, 137205 (2005).
  - [24] J. Shi, G. Vignale, D. Xiao, and Q. Niu, Quantum theory of orbital magnetization and its generalization to interacting systems, *Phys. Rev. Lett.* **99**, 197202 (2007).
  - [25] M. G. Lopez, D. Vanderbilt, T. Thonhauser, and I. Souza, Wannier-based calculation of the orbital magnetization in crystals, *Phys. Rev. B* **85**, 014435 (2012).
  - [26] J.-P. Hanke, F. Freimuth, A. K. Nandy, H. Zhang, S. Blügel, and Y. Mokrousov, Role of berry phase theory for describing orbital magnetism: From magnetic heterostructures to topological orbital ferromagnets, *Phys. Rev. B* **94**, 121114 (2016).
  - [27] R. Bianco and R. Resta, Orbital magnetization as a local property, *Phys. Rev. Lett.* **110**, 087202 (2013).
  - [28] S.-S. Wang, Y. Yu, J.-H. Guan, Y.-M. Dai, H.-H. Wang, and Y.-Y. Zhang, Boundary effects on orbital magnetization for a bilayer system with different chern numbers, *Phys. Rev. B* **106**, 075136 (2022).
  - [29] A. Marrazzo and R. Resta, Irrelevance of the boundary on the magnetization of metals, *Phys. Rev. Lett.* **116**, 137201 (2016).
  - [30] S.-S. Wang, Y.-M. Dai, H.-H. Wang, H.-C. Chen, B. Zhang, and Y.-Y. Zhang, Orbital magnetization under electric field and orbital magnetoelectric polarizability for a bilayer chern system, *Phys. Rev. B* **107**, 125135 (2023).
  - [31] D. Seleznev and D. Vanderbilt, Towards a theory of surface orbital magnetization, *Phys. Rev. B* **107**, 115102 (2023).
  - [32] A. Weiße, G. Wellein, A. Alvermann, and H. Fehske, The kernel polynomial method, *Reviews of Modern Physics* **78**, 275 (2006), publisher: American Physical Society.
  - [33] J. H. García, L. Covaci, and T. G. Rappoport, Real-Space Calculation of the Conductivity Tensor for Disordered Topological Matter, *Physical Review Letters* **114**, 116602 (2015), publisher: American Physical Society.
  - [34] A. Ferreira and E. R. Mucciolo, Critical delocalization of chiral zero energy modes in graphene, *Phys. Rev. Lett.* **115**, 106601 (2015).
  - [35] S. M. João, M. Andelković, L. Covaci, T. G. Rappoport, J. M. V. P. Lopes, and A. Ferreira, KITE: high-performance accurate modelling of electronic structure and response functions of large molecules, disordered crystals and heterostructures, *Royal Society Open Science* **7**, 191809 (2020).
  - [36] Z. Fan, J. H. Garcia, A. W. Cummings, J. E. Barrios-Vargas, M. Panhans, A. Harju, F. Ortmann, and S. Roche, Linear scaling quantum transport methodologies, *Physics Reports* **903**, 1 (2021).
  - [37] J. P. Santos Pires, S. M. João, A. Ferreira, B. Amorim, and J. M. Viana Parente Lopes, Anomalous transport signatures in weyl semimetals with point defects, *Phys. Rev. Lett.* **129**, 196601 (2022).
  - [38] S. G. de Castro, J. a. M. V. P. Lopes, A. Ferreira, and D. A. Bahamon, Fast fourier-chebyshev approach to real-space simulations of the kubo formula, *Phys. Rev. Lett.* **132**, 076302 (2024).
  - [39] L. M. Canonico, J. H. Garcia, and S. Roche, Orbital hall responses in disordered topological materials, *Phys. Rev. B* **110**, L140201 (2024).
  - [40] R. Cardias, H. U. R. Strand, A. Bergman, A. B. Klautau, and T. G. Rappoport, Real-space first-principles approach to orbitronic phenomena in metallic multilayers, *arXiv:2508.14270 [cond-mat.mtrl-sci]* (2025).
  - [41] F. D. M. Haldane, Model for a quantum hall effect without landau levels: Condensed-matter realization of the "parity anomaly", *Phys. Rev. Lett.* **61**, 2015 (1988).
  - [42] Supplementary material.
  - [43] A. Kitaev, Anyons in an exactly solved model and beyond, *Annals of Physics* **321**, 2 (2006).
  - [44] A.-L. He, L.-R. Ding, Y. Zhou, Y.-F. Wang, and C.-D. Gong, Quasicrystalline chern insulators, *Phys. Rev. B* **100**, 214109 (2019).
  - [45] Y.-k. Chen, Q.-h. Liu, B. Zou, and Y. Zhang, Kitaev formula for periodic, quasicrystal, and fractal floquet topological insulators, *Phys. Rev. B* **107**, 054109 (2023).
  - [46] J. He, Y.-X. Zhu, Y.-J. Wu, L.-F. Liu, Y. Liang, and S.-P. Kou, Zero modes around vacancies in topological insulators and topological superconductors on the honeycomb lattice with particle-hole symmetry, *Phys. Rev. B* **87**, 075126 (2013).
  - [47] R. Bianco and R. Resta, Mapping topological order in coordinate space, *Phys. Rev. B* **84**, 241106 (2011).
  - [48] D. Ceresoli, T. Thonhauser, D. Vanderbilt, and R. Resta, Orbital magnetization in crystalline solids: Multi-band insulators, chern insulators, and metals, *Phys. Rev. B* **74**, 024408 (2006).

# Supplementary Material For “Real-Space Spectral Approach to Orbital Magnetization”

## I. ORBITAL MAGNETIZATION SPECTRAL DENSITY

The orbital magnetization spectral density is defined as  $m_z(E) = \text{Tr}[\hat{\mathcal{M}}_z \delta(E - \hat{H})]$ . To evaluate this quantity efficiently, we expand the Dirac-delta operator in terms of Chebyshev polynomials of the Hamiltonian matrix. Technically, this requires first rescaling the Hamiltonian and energy variable according to  $\hat{H} \rightarrow \tilde{H}$  and  $E \rightarrow \tilde{E}$ , ensuring that the dimensionless energy falls within the canonical interval,  $\mathcal{I} = [-1, 1]$ , of orthogonal polynomial expansions. This approach involves computing moments of the resulting Chebyshev expansion. The total orbital magnetization  $M_z(E_F)$  is finally obtained by integrating  $m_z(E)$  up to the Fermi energy  $E_F$ , as outlined in the main text. In Fig. S1, we consider the three representative cases addressed in the main text. Panels (a), (b) and (c) of Fig. S1 use, respectively, the set of parameters of panels (b), (c) and (d) of Fig. 1 (main text).

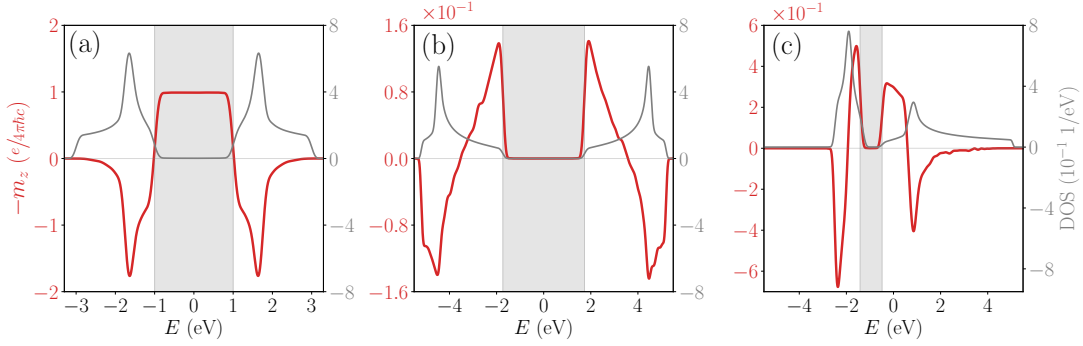


FIG. S1. (a-c) Orbital magnetization spectral density (red lines) in real-space formulation and density of states (gray lines) as functions of the energy. Panels (a), (b), and (c) show results for the systems with  $(\phi, \Delta/t_2) = (0.5\pi, 0)$ ,  $(0.5\pi, 6\sqrt{3})$ , and  $(0.1\pi, 3)$ , respectively. Calculations are performed on a rectangular domain with  $10^6$  sites. Chebyshev parameters:  $M = 200$  and  $R = 800$ .

For the topological insulating phase with  $\phi = 0.5\pi$  and  $\Delta/t_2 = 0$ , corresponding to Fig. S1(a), the orbital magnetization spectral density exhibits a well-defined plateau within the gap. This plateau has a sign opposite to that of  $m_z(E)$  in the metallic regime. In contrast, for the non-topological insulating phases shown in Figs. S1(b) and (c), the orbital magnetization spectral density vanishes within the gap. In particular, phases with  $\phi \neq 0.5\pi$  have broken particle-hole symmetry and, consequently, integrated spectral function over the valence band yields a non-zero orbital magnetization; see Fig. S1(c) together with Fig. 1(d) of the main text.

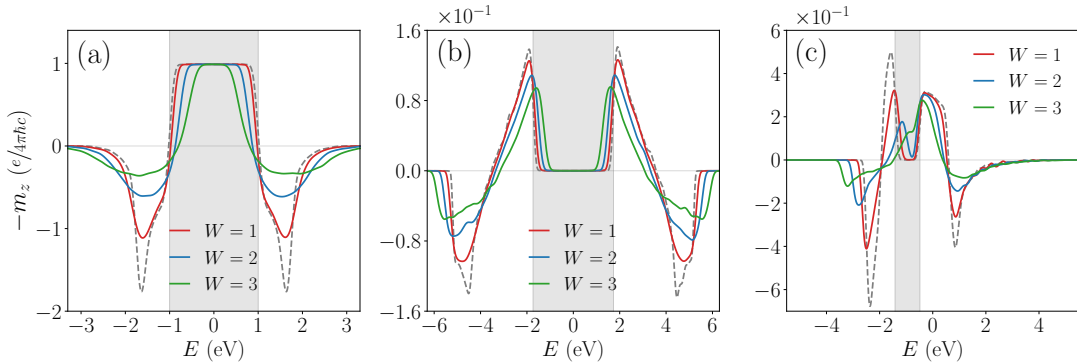


FIG. S2. Disorder effects on the Haldane model: The panels (a), (b) and (c) concern the red points in  $(\phi, \Delta/t_2) = (0.5\pi, 0)$ ,  $(0.5\pi, 6\sqrt{3})$  and  $(0.1\pi, 3)$  of the Fig. 1(a), respectively. (a-c) Energy dependence of orbital magnetization spectral density for selected Anderson disorder strengths:  $W = 1$  eV (red),  $W = 2$  eV (blue) and  $W = 3$  eV (green). The dashed gray lines correspond to the pristine systems. Simulation parameters as in Fig. S1.

Figures S2 show that weak Anderson disorder broadens the features of energy-resolved orbital magnetization spectral

density as expected. Thus, the smaller the gap, the less robust the features are to disorder. When the disorder strength exceeds the (pristine) energy gap scale, the impact of disorder is quite significant [see e.g. Fig. S2 (c)].

The real-space approach based on accurate Chebyshev polynomial expansions enables the calculation of the global Chern number via the derivative of the orbital magnetization with respect to the Fermi energy,  $\frac{dM_z}{dE_F}$ . By construction, this quantity is the energy-resolved orbital magnetization spectral density,  $m_z(E_F)$ . Hence,  $m_z(E_F)$  itself encodes information about the global Chern number of the system. Specifically, its value in the spectral gap is directly proportional to the Chern number of occupied states,  $m_z(E_F = 0) = -\left(\frac{e}{2\hbar c}\right) \frac{C}{2\pi}$ . Therefore, for a Chern number  $C = 1$ , the rescaled magnetization spectral density has a value of approximately  $-0.02 \mu_B/\text{eV}\text{\AA}^2$  across the band gap.

## II. SPECTRAL FUNCTION OF THE LOCAL ATOMIC ENVIRONMENT

We now examine the spatial structure of the orbital magnetization in real space. We begin with clean samples and later introduce disorder. The Hamiltonian parameters correspond to the three representative cases marked by red points in Fig. 1(a) of the main text.

Figure S3(a) shows the finite flake used in this analysis: a rectangular geometry with 100 sites along the zigzag direction and 200 sites along the armchair direction. To illustrate the origin dependence of local quantities involving the position operator, we compute the spatially resolved expectation value  $\langle \hat{\mathcal{M}}_z(\mathbf{r}) \rangle$  for a clean topological sample with  $\Delta/t_2 = 0$  and  $\phi = \pi/2$ .

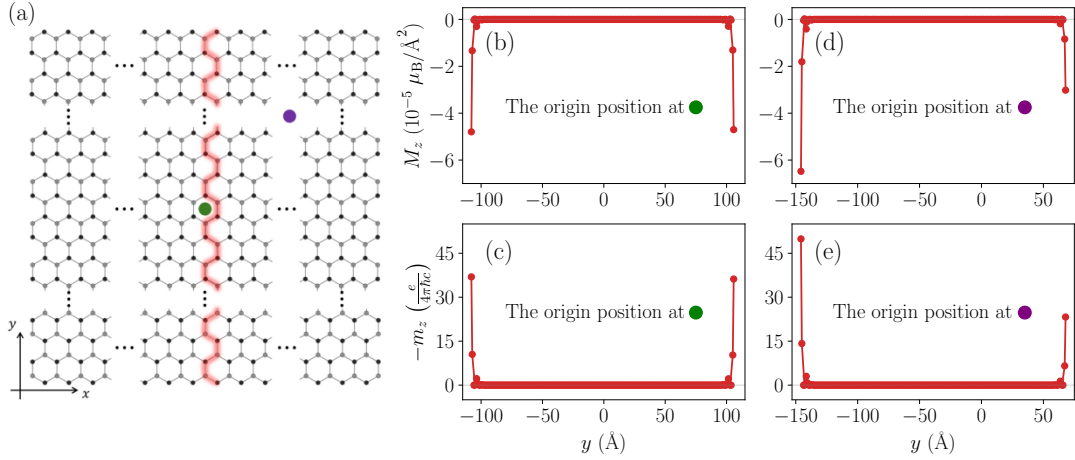


FIG. S3. (a) A flake with a rectangular geometry, composed of  $1 \times 10^4$  sites, representing the honeycomb lattice of the Haldane model. Black and grey circles indicate nonequivalent sites. (b)-(e) One-dimensional plots of the local orbital magnetization and local Chern number at  $E_F = 0$  eV for the 200 sites along the vertical red line shown in (a). Here we set  $\Delta/t_2 = 0$  and  $\phi = 0.5\pi$ , which corresponds to the topological insulating phase. The coordinate origin location chosen in each panel (b)-(e) is marked by the green [purple] point in panel (a).

Panels (b) and (d) of Fig. S3 show the profile of  $\langle \hat{\mathcal{M}}_z(\mathbf{r}) \rangle$  along the vertical line highlighted in panel (a). When the coordinate origin is chosen at the geometric center (green point), the two edges display identical contributions, as required by symmetry. When the origin is shifted away from the center (purple point), the two edges become inequivalent. This dependence is expected: because  $\hat{\mathcal{M}}_z$  contains the position operators explicitly,  $\langle \hat{\mathcal{M}}_z(\mathbf{r}) \rangle$  is origin dependent, while the spatial average defining the total orbital magnetization is completely origin independent.

Panels (c) and (e) show the corresponding *local orbital magnetization spectral density*. This quantity also varies with the coordinate origin, again reflecting the gauge dependence inherent to real-space expressions containing the position operator. For the topological insulating case, the spectral density vanishes in the bulk and acquires significant weight at the edges. Its spatial average is quantized and equal to the global Chern number, whereas for the non-topological insulating phase the spectral density vanishes everywhere.

It is useful to contrast this behavior with the construction of the local topological marker introduced by Bianco and Resta [47]. Their marker is engineered to be a bulk quantity even in finite samples: the insertion of  $\mathcal{P}$  and  $\mathcal{Q} = 1 - \mathcal{P}$  suppresses the matrix elements of the position operator that connect bulk and edge subspaces. As a consequence, the local marker is well defined and convergent only in the interior of a large sample; near the physical boundaries it becomes large and eventually diverges, reflecting the fact that it is not intended to describe edge physics. In our



case, however, the edge contributions are *not* pathologies to be projected out. For orbital magnetization in a finite Chern insulator, the boundary states carry the spectral flow responsible for the linear dependence of  $M_z(E_F)$  observed in the main text. The quantity plotted in Fig. S3 therefore represents the actual spatial distribution of the orbital magnetization spectral density, not a local topological invariant. We now turn to the effect of Anderson disorder,

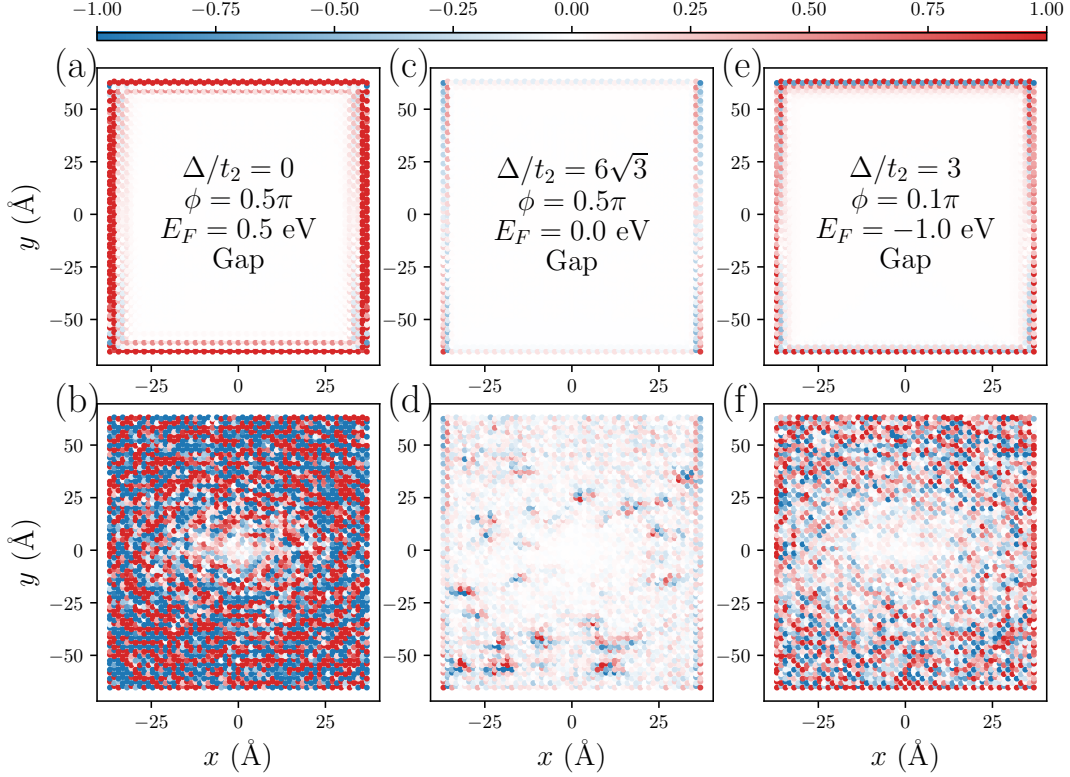


FIG. S4. Local orbital magnetization, displaying only values in the range  $[-1, 1] \mu_B$ , in real space for a system composed of  $3.6 \times 10^3$  sites with a rectangular geometry. First row: pristine systems. Second row: systems with Anderson disorder ( $W = 2$  eV). The panels (a) and (b) correspond to the topological insulating phase ( $\phi = 0.5\pi, \Delta/t_2 = 0$ ) with  $E_F = -0.5$  eV and 0, respectively; the panels (c) and (d) correspond to the non-topological insulating phase ( $\phi = 0.5\pi, \Delta/t_2 = 6\sqrt{3}$ ) with  $E_F = 0$ ; and the panels (e) and (f) correspond to the non-topological insulating phase ( $\phi = 0.1\pi, \Delta/t_2 = 3$ ) with  $E_F = -1$  eV. The red (blue) points correspond to positive (negative) orbital magnetization. We used 200 Chebyshev polynomials.

complementing the results of the main text. Figure S4(b) shows that in the topological insulating phase the orbital magnetization remains delocalized throughout the sample and is remarkably robust against disorder. In contrast, for the trivial insulating phase with a large gap, disorder induces isolated mid-gap states that manifest as small, spatially localized patches of orbital magnetization [panel (d)]. When the disorder strength becomes comparable to the gap, these localized regions expand and the orbital magnetization spreads across the sample [panel (f)], consistent with a transition toward an Anderson insulating or critical regime.

These results illustrate how disorder modifies the spatial structure of the orbital magnetization in distinct ways depending on the underlying phase, while preserving the global behavior of  $M_z$  discussed in the main text.

### III. FURTHER TEST CASES FOR ORBITAL MAGNETIZATION

This section further showcases our spectral real-space approach by presenting additional representative cases and comparing the results against those derived from the reciprocal space formula of the modern theory of orbital magnetization. These comparisons serve to underscore the computational practicality and effectiveness of our real-space approach to calculate this fundamental property in crystalline materials.

Figure S5(b) compares our real-space results, obtained using the Chebyshev expansion for  $\Delta/t_2 = 3$  across the range  $\phi = 0$  to  $\pi$ , with two established methods: the modern theory (bulk formula) in reciprocal space and the extrapolated results from finite-sample calculations (heuristic formula) of Fig. 7 in Ref. [48]. The results show excellent agreement

with our real-space approach based on Chebyshev polynomials.

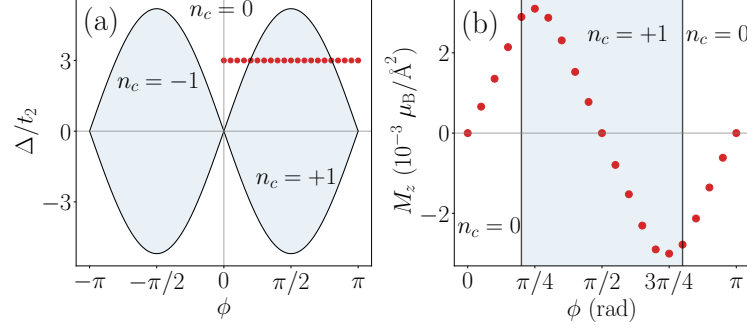


FIG. S5. Panel (a) illustrated the Chern number of the valence band of the Haldane model as a function of the parameters  $\phi$  and  $\Delta/t_2$  ( $t_1 = 2$  eV and  $t_2 = 1/3$  eV). The red points concern in the subsequent figure. (b) Orbital magnetization of the Haldane model with  $\Delta/t_2 = 3$  as a function of the parameter  $\phi$ , where the lowest band is treated as occupied. The system has nonzero Chern number in the region between two line vertical lines.

Figures S6(b)-(l) show plots of the Fermi energy dependence of the orbital magnetization for  $\Delta/t_2 = 3$  with  $\phi = 0, 0.1\pi, 0.2\pi, 0.3\pi, 0.4\pi, 0.5\pi, 0.6\pi, 0.7\pi, 0.8\pi, 0.9\pi$  e  $\pi$ , respectively, using our real-space formalism (red lines) and the reciprocal-space formalism (blue points). We observe that there are pairs of identical curves using  $\phi = 0.5\pi$  as a reference point. For example, the pair of curves for  $\phi = 0.3\pi$  and  $\phi = 0.7\pi$  are identical but exhibit inverted energy bands and a sign reversal in orbital magnetization.

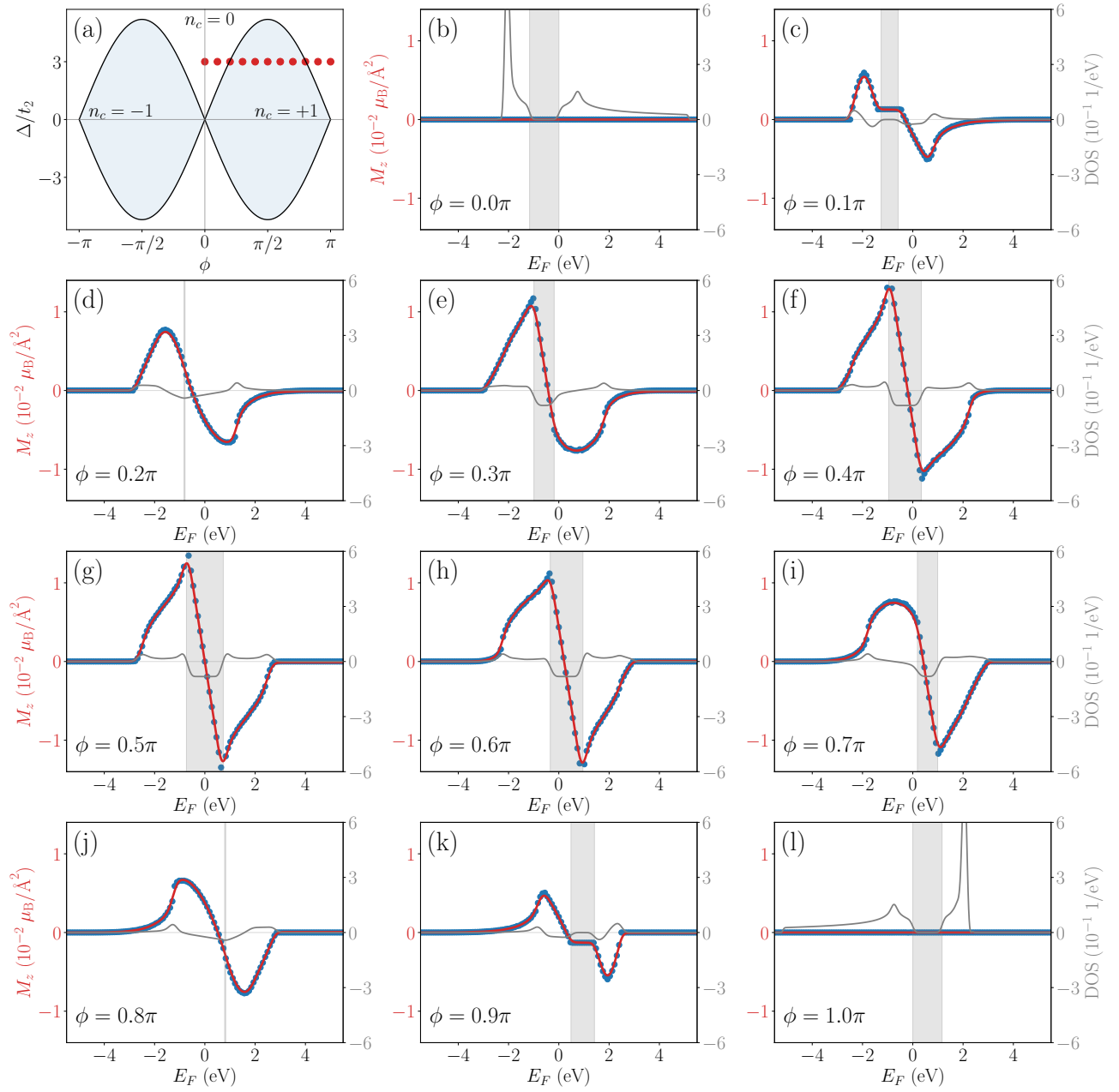


FIG. S6. Panel (a) illustrates the Chern number of the bottom band of the Haldane model as a function of the parameters  $\phi$  and  $\Delta/t_2$  ( $t_1 = 2$  eV and  $t_2 = 1/3$  eV). The red points concern the subsequent figures. (b)-(l) Orbital magnetization (red lines) in real-space formulation and density of states (gray lines) as functions of the energy,  $E_F$  and  $E$ , respectively. The blue points correspond to the orbital magnetization in the reciprocal-space formulation. In our spectral simulations, we used a real-space system composed of  $10^6$  sites (rectangular geometry) with 200 Chebyshev polynomials and 800 random vectors.